JOURNAL OF COMPUTATIONAL PHYSICS 58, 246–269 (1985)

Finite Element Solution of Maxwell's Equations for Hyperthermia Treatment Planning

DANIEL R. LYNCH, KEITH D. PAULSEN, AND JOHN W. STROHBEHN

Thayer School of Engineering, Dartmouth College, Hanover, New Hampshire 03755

Received December 13, 1983; revised March 23, 1984

A general Galerkin formulation is given for the periodic form of Maxwell's equations on a bounded inhomogeneous medium. The formulation conserves energy exactly and its dispersion relation is studied. Solutions for test problems representative of hyperthermia applications show good agreement with analytic solutions. A representative clinical example is shown. © 1985 Academic Press, Inc

INTRODUCTION

It has been known for at least a century that hyperthermia—elevated tissue temperature—has beneficial effects in cancer therapy. Until recently there has been little careful research in this area. However, recent positive results from heating cancer cells to 42°C or higher, alone or in combination with radiation or chemotherapy, have renewed interest in this form of treatment. (For a brief history, see Hahn [9] or Storm [31].)

Several approaches are possible for elevating the tissue temperature. Local heating may be produced invasively, e.g., by small microwave antennas inserted into the tumor through hypodermic needles; or noninvasively by ultrasound transducers for superficial tumors. Regional heating has also been pursued noninvasively by induction and microwave devices. An overview of research and clinical results can be found in the proceedings of recent international symposia [34, 5] as well as the monographs by Hahn [9] and Storm [31]. Several devices are now undergoing clinical evaluation.

Detailed thermal measurements are presently impractical, particularly for deep-seated tumors, and the problem of temperature prediction/inference is confronted in several areas, including the scientific documentation of experimental and clinical results; the design of equipment; and the selection of equipment, power levels, treatment times, etc., for a particular patient. This latter category we refer to as "treatment planning." It is our goal to create temperature prediction algorithms which can ultimately be used in a clinical setting with realistic patient geometry—preferably derived from *CT* scans or other clinical information.

The problem of temperature prediction is itself twofold: first, predict the rate of

0021-9991/85 $3.00

heat deposition in the various tissues; and second, predict the resultant temperatures. The latter problem is common to all of the heating devices and has been successfully formulated as a heat diffusion problem, with a pseudo-first-order decay term to represent the crucial role of blood circulation in temperature regulation. This "bioheat equation" has received considerable attention [1, 13], and its transient solution on complex geometries is tractable numerically, particularly with modern finite element techniques. The heat source calculations, however, tend to be device-specific. Since electromagnetic devices are quite common, we have pursued the solution of Maxwell's equations on finite elements, with the aim of using the same element grid for both heat source and temperature calculations.

Several significant finite element solutions for electromagnetic problems have been reported, as evidenced by the recent compilations [3, 30]. The bulk of the applications involve reduction of the governing equations to simpler Laplace, Poisson, or diffusion equations with subsequent solution on finite elements. In the latter category, major contributions have been made relative to magnetic field and eddy current analysis in electric machines [4, 27, 21, 22]. At the low frequency of commercial interest, displacement current is negligible and the diffusion equation governs; but significant complexity is introduced by the nonlinear B/H relationship encountered under typical operating conditions. This latter complication is unimportant in the hyperthermia–cancer problem; however, our interest is in the frequency range 10–100 MHz and displacement current may not be neglected. Further, the electrical properties do vary significantly with tissue type. Hence, we must solve the full Maxwell equations on a bounded, inhomogeneous domain.

In this paper, we present a general Galerkin formulation for the electric field. The global energy conservation property of the numerical solution is established, and the numerical dispersion relation is studied for the simplified Helmholtz equation to produce some guidelines for mesh design. Planar solutions are then obtained numerically and compared with analytic solutions for cases inspired by two regional hyperthermia devices currently in use. Finally, a realistic clinical application is shown.

Governing Equations and Discretization

Our starting point is Maxwell's equations, which have been reviewed in the present context by Strohbehn and Roemer [35]. Assuming a periodic solution in time of the form $\exp(-i\omega t)$, we have

$$\nabla \times \mathbf{E} = i\omega\mu\mathbf{H} \tag{1a}$$

$$\nabla \times \mathbf{H} = -i\omega\varepsilon_c\mathbf{E} \tag{1b}$$

where

$\mathbf{E}$ is the time-invariant complex amplitude of the electric field
$\mathbf{H}$ is the time-invariant complex amplitude of the magnetic field
μ is the magnetic permeability
$\varepsilon_c = \varepsilon + i\sigma/\omega$ is the complex permittivity
σ is the electric conductivity
ε is the permittivity
ω is the radian frequency
$i = \sqrt{-1}$.

As noted by Strohbehn and Roemer [35], μ is effectively constant in tissue; while σ and ε vary with both frequency and tissue type. Some typical values of these parameters are listed in Table I.

Since the power deposited per unit volume of tissue is given by $\sigma |\mathbf{E}|^2/2$, our objective is to compute the electric field directly. Therefore we isolate $\mathbf{E}$ by a standard maneuver: take the curl of Eq. (1a), and substitute (1b). The result, taking advantage of the fact that μ is a constant, is

$$\nabla \times (\nabla \times \mathbf{E}) - k^2 \mathbf{E} = 0 \tag{2}$$

TABLE I

Representative Values of Dielectric Constant and Electric Conductivity at Various Frequencies[a]

	13 MHz	40 MHz	70 MHz	100 MHz
Muscle				
$\varepsilon/\varepsilon_0$	122.	97.3	85.	72.
σ	0.60	0.693	0.802	0.889
Lung				
$\varepsilon/\varepsilon_0$	3.2	30.	40.	40.
σ	0.007	0.15	0.35	0.35
Fat				
$\varepsilon/\varepsilon_0$	28.	14.6	10.5	10.5
σ	0.20	0.20	0.21	0.22
Bone				
$\varepsilon/\varepsilon_0$	28.	7.86	10.	10.
σ	0.20	0.02	0.02	0.02
Heart				
$\varepsilon/\varepsilon_0$	140.	70.	89.	89.
σ	0.6	0.76	0.93	0.93
Deionized water				
$\varepsilon/\varepsilon_0$	70.	70.	78.	78.
σ	0.	0.	0.	0.

[a] $\varepsilon_0 = 8.854 \times 10^{-12}$ F/m; $\mu = \mu_0 = 4\pi \times 10^{-7}$ H/m; σ expressed in mho/m. Values were assembled with some discretion from Hill *et al.* [11]; Young *et al.* [37]; Iskander *et al.* [12]; Guy *et al.* [8]; Schwan and Foster [28]; Lin *et al.* [15]; Hahn *et al.* [10]; Burdette [2].

where k is the complex wavenumber:

$$k^2 = \omega^2 \mu \varepsilon_c = \omega^2 \mu \varepsilon + i\omega\mu\sigma. \tag{3}$$

Our approximate solution is based on the weak form of (2)

$$\langle [\nabla \times (\nabla \times \mathbf{E})]\, \phi_i \rangle - \langle k^2 \mathbf{E} \phi_i \rangle = 0, \tag{4}$$

where $\langle\ \rangle$ indicates integration over the volume, and ϕ_i is any scalar function. The first term in (4) may be integrated by parts,

$$\begin{aligned} \langle [\nabla \times (\nabla \times \mathbf{E})]\, \phi_i \rangle &= \langle \nabla \times (\phi_i \nabla \times \mathbf{E}) \rangle - \langle \nabla \phi_i \times (\nabla \times \mathbf{E}) \rangle \\ &= \oint \mathbf{n} \times (\phi_i \nabla \times \mathbf{E})\, ds - \langle \nabla \phi_i \times (\nabla \times \mathbf{E}) \rangle \end{aligned} \tag{5}$$

and the weak form which we utilize is thus

$$\langle (\nabla \times \mathbf{E}) \times \nabla \phi_i \rangle - \langle k^2 \mathbf{E} \phi_i \rangle = i\omega\mu \oint \mathbf{H} \times \mathbf{n} \phi_i\, ds. \tag{6}$$

Note that we have purposefully reintroduced $\mathbf{H}$ in the boundary integral. This term is the vehicle for applying boundary conditions where $\mathbf{E}$ is not specified; and for computing $\mathbf{n} \times \mathbf{H}$ on boundaries where $\mathbf{E}$ is specified.

To complete the numerical discretization we expand the unknown $\mathbf{E}$ in terms of the real-valued weighting functions ϕ_i

$$\mathbf{E} = \sum_{j=1}^{N} \mathbf{E}_j \phi_j \tag{7}$$

and require the satisfaction of (6) for $i = 1$ through N. This Galerkin approximation is then implemented on conventional finite elements, where ϕ_i and $\mathbf{E}$ are continuous with piecewise continuous first derivatives. When $\mathbf{E}$ is in the plane of analysis an essential discontinuity is required at internal boundaries where ε_c changes abruptly. Our finite element discretization is formally severed along these boundaries, and the appropriate conditions enforced. Since $\mathbf{n} \times \mathbf{H}$ must be continuous, the boundary integrals in (6) mutually cancel along such boundaries. These properties allow assembly of Eqs. (6) in the usual element-by-element manner.

For a discretization of N nodes of which M lie on the boundary, Eqs. (6) constitute N equations in $N+M$ unknowns: N values of $\mathbf{E}_j$ and M values of $\mathbf{F}_i \equiv \oint \mathbf{H} \times \mathbf{n} \phi_i\, ds$. To these equations we add a boundary condition (BC) on either $\mathbf{E}_i$ or $\mathbf{F}_i$ at each boundary node, which closes the system algebraically. Operationally, when $\mathbf{F}_i$ is known it simply constitutes the right side of Eq. (6_i). When $\mathbf{E}_i$ is known, Eq. (6_i) is removed from the matrix in favor of the BC, and saved. Following the simultaneous determination of the $\mathbf{E}_j$, the unknown $\mathbf{F}_j$ are computed directly via

the saved equations. In this way we enforce all of the Galerkin equations (6), a feature which will be essential in demonstrating the energy balance below.[1]

The time-averaged energy flux $\mathbf{P}_{av}$ is given analytically as

$$\mathbf{P}_{av} = \mathrm{Re}(\mathbf{P}) = \mathrm{Re}\left(\frac{\mathbf{E}\times\mathbf{H}^*}{2}\right) \tag{8}$$

where $\mathbf{P} = \frac{1}{2}\mathbf{E}\times\mathbf{H}^*$ is the complex Poynting vector. Equation (8) may be integrated over the boundary by a simple dot product of the computed $\mathbf{E}_j$ and $\mathbf{F}_j$:

$$\sum_{j=1}^{N} \mathbf{F}_j^* \cdot \mathbf{E}_j = \oint (\mathbf{H}^*\times\mathbf{n})\cdot\left(\sum_{1}^{N}\mathbf{E}_j\phi_j\right) ds = \oint (\mathbf{H}^*\times\mathbf{n})\cdot\mathbf{E}\, ds$$

$$= \oint (\mathbf{E}\times\mathbf{H}^*)\cdot\mathbf{n}\, ds. \tag{9}$$

Thus the total power consumption is given by

$$-\oint \mathbf{P}_{av}\cdot\mathbf{n}\, ds = -\mathrm{Re}\left[\sum_{1}^{N}\mathbf{F}_j^*\cdot\mathbf{E}_j/2\right]. \tag{10}$$

Of course, the summation need be carried over boundary nodes only, since otherwise $\mathbf{F}_j = 0$ by definition. Below we show that this simple calculation is algebraically identical to the volume integral of the resistive power loss obtained from the numerical $\mathbf{E}$ field.

Finally we note that for the special case when $\mathbf{E} = E_z(x, y)\,\mathbf{z}$, formulation (6) reduces to a simple scalar Galerkin–Helmholtz equation,

$$\langle \nabla E_z\cdot\nabla\phi_i\rangle - \langle k^2 E_z\phi_i\rangle = \oint \nabla E_z\cdot\mathbf{n}\phi_i\, ds \tag{11}$$

with

$$\nabla E_z\cdot\mathbf{n} = i\omega\mu(\mathbf{H}\times\mathbf{n})\cdot\mathbf{z} \tag{12}$$

and ∇, $\mathbf{H}$, and $\mathbf{n}$ restricted to the (x, y) plane.

[1] A more conventional finite element practice would be to ignore Eq. (6,) when $\mathbf{E}_i$ is known, which also eliminates the variable $\mathbf{F}_i$ from the system. While the computed $\mathbf{E}_j$ values would be unchanged, essential information for computing the exact energy flux is lost. Lynch [18] shows that for a simple 1-D scalar wave equation, this conventional approach results in an error which is first order in the mesh spacing.

ENERGY BALANCE

The general statement of energy conservation for Eqs. (1a), (1b) is (Jordan and Balmain, [14])

$$\frac{d}{dt}\left\langle \frac{\mu \mathscr{H}\cdot\mathscr{H}}{2}+\frac{\varepsilon \mathscr{E}\cdot\mathscr{E}}{2}\right\rangle + \langle \sigma \mathscr{E}\cdot\mathscr{E}\rangle + \oint (\mathscr{E}\times\mathscr{H})\cdot \mathbf{n}\, ds = 0, \tag{13}$$

where $\mathscr{H} = \mathrm{Re}[\mathbf{H}\exp(-i\omega t)]$, $\mathscr{E} = \mathrm{Re}[\mathbf{E}\exp(-i\omega t)]$, and $\mathscr{P} = \mathscr{E}\times\mathscr{H}$ is the Poynting vector. In terms of the complex amplitudes $\mathbf{H}$ and $\mathbf{E}$, two conditions must be satisfied:

$$\left\langle \frac{\sigma \mathbf{E}\cdot\mathbf{E}^*}{2}\right\rangle + \mathrm{Re}\oint \left(\frac{\mathbf{E}\times\mathbf{H}^*}{2}\right)\cdot \mathbf{n}\, ds = 0 \tag{14}$$

and

$$\left\langle -\frac{\omega\mu}{2}\mathbf{H}\cdot\mathbf{H}^* + \frac{\omega\varepsilon}{2}\mathbf{E}\cdot\mathbf{E}^*\right\rangle + \mathrm{Im}\oint \left(\frac{\mathbf{E}\times\mathbf{H}^*}{2}\right)\cdot \mathbf{n}\, ds = 0. \tag{15a}$$

Equation (14) represents the familiar time-averaged energy balance between ohmic heating in the volume and energy flux across the surface; (15a) represents the energy balance for the reactive power, which accounts for periodic changes in stored energy. Since we do not compute $\mathbf{H}$ on the interior, we utilize (1a) in the volume integral of (15) to obtain the equivalent form

$$\left\langle \frac{-1}{2\omega\mu}(\nabla\times\mathbf{E})\cdot(\nabla\times\mathbf{E}^*) + \frac{\omega\varepsilon}{2}\mathbf{E}\cdot\mathbf{E}^*\right\rangle + \mathrm{Im}\oint \left(\frac{\mathbf{E}\times\mathbf{H}^*}{2}\right)\cdot \mathbf{n}\, ds = 0. \tag{15b}$$

While our numerical solution only approximately satisfies Maxwell's equations at a point, nevertheless it does exactly satisfy the global relations (14) and (15b). To see this, take the dot product of Eq. (6) with $\mathbf{E}_i^*$ and sum from $i = 1$ to N. The first term on the left yields, after rearrangement of the triple product,

$$\left\langle \sum_i (\nabla\phi_i\times\mathbf{E}_i^*)\cdot(\nabla\times\mathbf{E})\right\rangle$$

and since from Eq. (7) we have $\nabla\times\mathbf{E}^* = \sum_i \nabla\phi_i\times\mathbf{E}_i^*$, this term is identically $\langle(\nabla\times\mathbf{E})\cdot(\nabla\times\mathbf{E}^*)\rangle$. The second term on the left yields $\langle k^2\mathbf{E}\cdot\mathbf{E}^*\rangle$ directly. The right side of (6) yields, after rearranging the triple product,

$$i\omega\mu\oint(\mathbf{E}^*\times\mathbf{H})\cdot\mathbf{n}\, ds.$$

Assembling these results and dividing by $2i\omega\mu$ thus yields

$$\left\langle \frac{1}{i\omega\mu}\frac{(\nabla\times\mathbf{E})\cdot(\nabla\times\mathbf{E}^*)}{2}+i\omega\varepsilon\frac{\mathbf{E}\cdot\mathbf{E}^*}{2}-\sigma\frac{\mathbf{E}\cdot\mathbf{E}^*}{2}\right\rangle=\oint\left(\frac{\mathbf{E}^*\times\mathbf{H}}{2}\right)\cdot\mathbf{n}\,ds. \tag{16}$$

Noting that $(\mathbf{E}^*\times\mathbf{H})$ is the conjugate of $(\mathbf{E}\times\mathbf{H}^*)$, the real part of (16) is

$$\left\langle\sigma\frac{\mathbf{E}\cdot\mathbf{E}^*}{2}\right\rangle+\mathrm{Re}\oint\left(\frac{\mathbf{E}\times\mathbf{H}^*}{2}\right)\cdot\mathbf{n}\,ds=0 \tag{17a}$$

which is identical to its analytic counterpart (14). Thus the time-averaged portion of the energy balance is satisfied exactly by the numerical solution. As described above, the numerical power input in (17a) may be efficiently computed according to (10), thus avoiding the necessity of computing the volume integral of the ohmic heating.

The imaginary part of (16) is

$$\left\langle-\frac{1}{2\omega\mu}(\nabla\times\mathbf{E})\cdot(\nabla\times\mathbf{E}^*)+\frac{\omega\varepsilon}{2}\mathbf{E}\cdot\mathbf{E}^*\right\rangle+\mathrm{Im}\oint\left(\frac{\mathbf{E}\times\mathbf{H}^*}{2}\right)\cdot\mathbf{n}\,ds=0 \tag{17b}$$

which exactly reproduces the reactive power balance (15b). We conclude that the numerical solution conserves energy exactly.

Dispersion Analysis

In an unbounded, homogeneous medium Eq. (2) admits plane wave solutions of the form $\mathbf{E}_0\exp(iks)$, where $s=\mathbf{r}\cdot\mathbf{n}$, $\mathbf{n}$ is the unit vector in the direction of propagation, and k is related to the forcing frequency ω by the dispersion relation (3). In this section we develop the dispersion relation which governs the numerical solution on the uniform element configurations of Figs. 1 and 5, and explore its fidelity to its analytic counterpart. We treat only the case where $\mathbf{E}$ is normal to the (x, y) plane, governed by Eq. (11). Mullen and Belytschko [23] have studied the lossless ($\sigma=0$) form and report numerical wave speed ($\hat{\omega}/k$, where $\hat{\omega}$ is the numerical frequency) as a function of real wavenumber k, for a variety of 2-D grids. In our case we wish to study the forced response at given real frequency ω. Thus we invert the question: given ω, find the numerical wavenumber $\hat{k}$ and compare it with the analytic value k. Platzman [26] has examined Eq. (11) in this way for the lossless case, and discovered additional complex values of $\hat{k}$ corresponding to parasitic solutions. In a dissipative system, both $\hat{k}$ and k will be complex even for the nonparasitic modes, and we adopt two measures of fidelity:

(a) the numerical wavelength $\hat{L}=2\pi/\mathrm{Re}(\hat{k})$, divided by its analytic counterpart—this ratio is identical to the wave speed ratio

$$\frac{\hat{L}}{L}=\frac{\mathrm{Re}(k)}{\mathrm{Re}(\hat{k})}; \tag{18}$$

(b) the numerical damping rate, $-\mathrm{Im}(\hat{k})$. In this case we report the amplitude decrease over one analytic wavelength, divided by its analytic counterpart

$$\delta = \exp[-\mathrm{Im}(\hat{k}-k)\,L]. \tag{19}$$

This measure is analogous to the "propagation factor" commonly employed in the dispersion analysis of traveling waves with real wavenumber (e.g., Gray and Lynch [7]).

It is readily verified that for the triangulation of Fig. 1, Eq. (11) weighted by ϕ_1 is

$$\frac{A}{h^2}\left[8E_{z1} - \frac{4}{3}\sum_2^7 E_{zj}\right] - k^2 A\left[E_{z1} + \frac{1}{6}\sum_2^7 E_{zj}\right] = 0. \tag{20}$$

Assuming a solution of the form $E_{zj} = E_{z0}\exp(i\hat{k}x_j)$, i.e., a wave parallel to the x axis, Eq. (20) yields the requirement

$$\lambda + \frac{1}{\lambda} = \frac{2 - 2K^2/3}{1 + K^2/6} \tag{21}$$

where $K \equiv ka$, a is the mesh spacing in the x direction (Fig. 1), and λ is the ratio of the numerical solution at adjacent nodes,

$$\lambda \equiv \exp(i\hat{k}a). \tag{22}$$

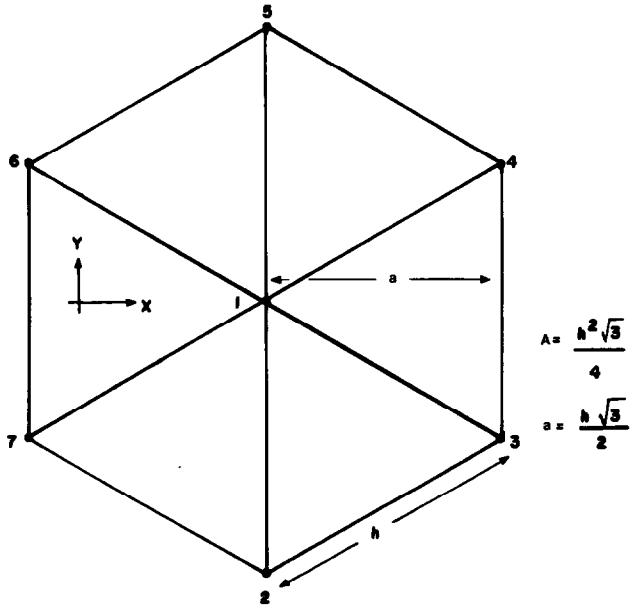

FIG. 1. Uniform grid of equilateral triangles employed in the dispersion analysis.

Equation (21) is identical to that which governs a one-dimensional discretization on linear elements. The two roots will be such that $\lambda_2 = 1/\lambda_1$, i.e., $\hat{k}_2 = -\hat{k}_1$, corresponding to progressive and regressive waves along the x axis. The solution for λ is

$$\lambda = \left(\frac{1 - K^2/3}{1 + K^2/6}\right) \pm i\sqrt{1 - \left(\frac{1 - K^2/3}{1 + K^2/6}\right)^2}. \tag{23}$$

It is readily verified that for the lossless case (K real) $|\lambda| = 1$ for all frequencies below the cutoff point $K \leqslant \pi$. Thus the numerical solution in this case provides no artificial damping: $\delta = 1$.

In Fig. 2 we show both $\hat{L}/L$ and δ as a function of dimensionless frequency $W \equiv \omega a\sqrt{\mu\varepsilon}$, with dimensionless dissipation $S = \sigma a\sqrt{\mu/\varepsilon}$ as a parameter. As can be seen in Fig. 2a, the wavelength ratio is only slightly influenced by dissipation, and is very near to unity for $W/\pi \leqslant 0.1$. On the other hand, the damping rate δ deteriorates with increasing S or W; and yields good accuracy (roughly 1%) in the range $WS \leqslant 0.02$. It is interesting to note that these approximate guidelines for mesh design can also be obtained by requiring (a) 20 or more elements per undamped analytic wavelength ($W/\pi \leqslant 0.1$); and (b) 10 or more elements per factor of e decay in the heavily damped analytic case.

For a wave in the y direction, $E_{zj} = E_{z0}\exp(i\hat{k}y_j)$, Eq. (20) produces the fourth-order polynomial

$$\left(\gamma + \frac{1}{\gamma}\right)^2 + 2\left(\gamma + \frac{1}{\gamma}\right) + \left(\frac{4\mathscr{K}^2 - 16}{\mathscr{K}^2 + 2}\right) = 0 \tag{24}$$

where $\gamma \equiv \exp(i\hat{k}h/2)$ is the ratio of numerical amplitudes at adjacent nodes in the y

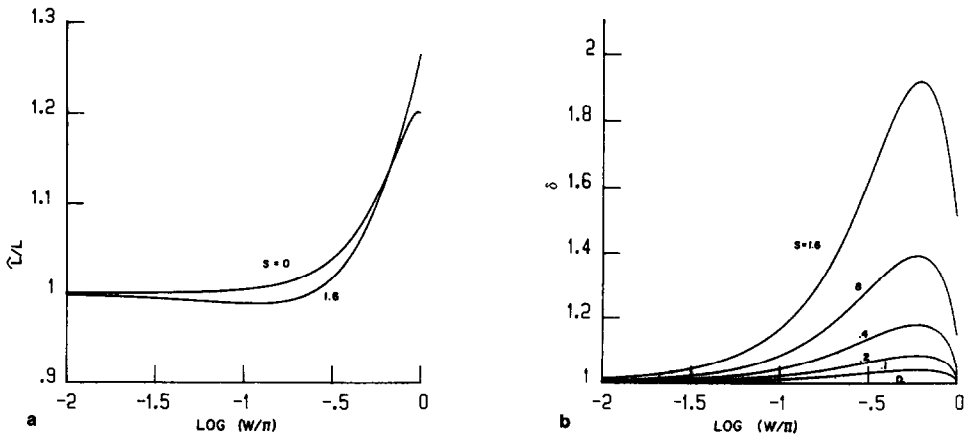

FIG. 2. Wavelength ratio (a) and damping ratio (b) for E_z wave in x direction, for the grid of Fig. 1. $W = \omega a\sqrt{\mu\varepsilon}$; $S = \sigma a\sqrt{\mu/\varepsilon}$.

direction and $\mathscr{K} \equiv kh/2$ is analogous to K in the x direction analysis ($\mathscr{K} = K/\sqrt{3}$). Equation (24) has four roots with the properties $\gamma_2 = 1/\gamma_1$; $\gamma_4 = 1/\gamma_3$,

$$\left(\gamma + \frac{1}{\gamma}\right) = -1 \pm R(\mathscr{K}) \tag{25a}$$

where

$$R(\mathscr{K}) \equiv + \sqrt{\frac{18 - 3\mathscr{K}^2}{2 + \mathscr{K}^2}}. \tag{25b}$$

In the limit as $\mathscr{K}$ vanishes, $R = 3$ and it is clear that the + option in (25a) yields progressive and regressive waves which correspond to the analytic solution

$$\gamma = \left(\frac{R-1}{2}\right) \pm i \sqrt{\left(\frac{3-R}{2}\right)\left(\frac{1+R}{2}\right)}. \tag{26}$$

For the lossless case, R is real for $\mathscr{K} \leqslant \sqrt{6}$, and $|\gamma| = 1$ in this range; i.e., the numerical solution introduces no artificial damping, $\delta = 1$. Values of $\hat{L}/L$ and δ are plotted in Fig. 3 for these physically meaningful waves. The curves are essentially indistinguishable from the X direction curves (Fig. 2) except at the low resolution end of the scale, $W \simeq \pi$, and thus the accuracy guidelines for W and WS are unchanged.

The "negative" option in (25a) yields two parasitic waves which have no counterpart in the analytic solution

$$\gamma_p = -\frac{1+R}{2} \pm \sqrt{\left(\frac{R-1}{2}\right)\left(\frac{R+3}{2}\right)}. \tag{27}$$

Again in the lossless case, R is real and exceeds unity for $\mathscr{K} < 2$, i.e., the entire

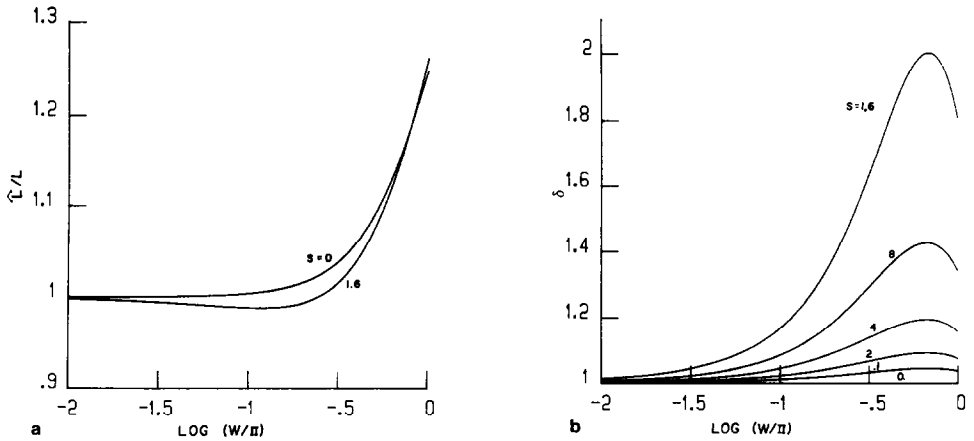

FIG. 3. Wavelength ratio (a) and damping ratio (b) for E_z wave in y direction, for the grid of Fig. 1.

range of reasonable resolution. In this range, both values of γ_p will be real and negative, and thus these modes will oscillate from node to node with wavelength h. Due to the arrangement of the grid of Fig. 1, these will also appear as an undamped wave of length $\hat{L} = 2a$ in the x direction when the dominant physical wave is in the y direction. Because the associated wavenumbers $\hat{k}$ are complex, these parasitic waves are frequently overlooked in dispersion analyses (e.g., [23]) which postulate a real valued k and find the corresponding $\hat{\omega}$. Platzman [26] has discussed similar numerical artifacts in a related study of the lossless case.

The attenuation rate per mesh spacing $|\gamma_{p+}|$ is insensitive to K and S and very strong. Over the range of physical interest, $S \leqslant 1.6$ and $K/\pi \leqslant 0.1$, we find that $|\gamma_{p+}| = 0.269 \pm 0.002$, and thus $|\gamma_{p+}|^3 < 0.02$. Further, for this range of K and S, the size of the imaginary part of γ_{p+} does not exceed 5% of its real part; that is, all the parasites in this range will have very short wavelengths.

For finite problems, the parasitic modes will originate in the fitting of the boundary conditions. Consider, for example, the termination of the uniform grid as in Fig. 4. Specification of E_z along the top and bottom will invoke all four modes, since E_z is constrained at four values of y. The rapid attenuation/growth of the parasites, combined with the requirement of finite E_z at the boundaries, implies that the parasites will effectively penetrate only three or four mesh spacings into the interior of the grid.

Finally, consider a homogeneous grid of bilinear elements as in Fig. 5. Equation (11), weighted by ϕ_1, yields in this case

$$\frac{K^2}{36}\left[16E_{z1} + \sum_{2}^{5} E_{zi} + 4\sum_{6}^{9} E_{zi}\right] + \frac{1}{6}\left[2\sum_{2}^{9} E_{zi} - 16E_{z1}\right] = 0. \tag{28}$$

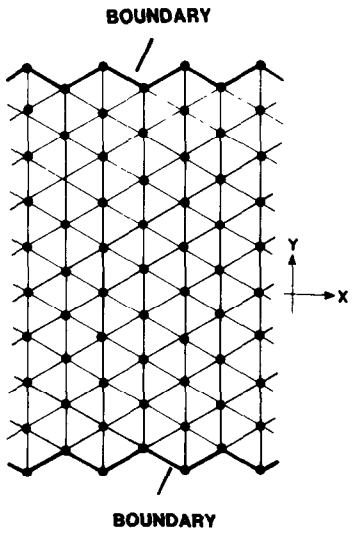

FIG. 4. Hypothetical termination of homogeneous triangulation.

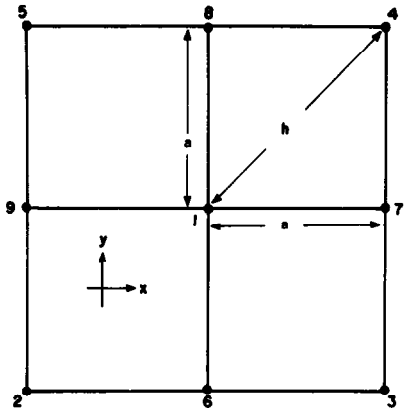

FIG. 5. Uniform bilinear grid for the dispersion analysis.

For waves in either the x or y direction, the dispersion relation is identical to (23), with no parasitic modes. All of the previous discussion of this equation and Fig. 2 are thus pertinent. For waves in any of the diagonal directions on the bilinear grid, (28) yields the requirement

$$\left(\gamma+\frac{1}{\gamma}\right)^2(K^2+12)+\left(\gamma+\frac{1}{\gamma}\right)(8K^2+24)+16(K^2-6)=0 \tag{29}$$

where $\gamma \equiv \exp(i\hat{k}h/2)$. Again there are two physically meaningful solutions,

$$\gamma+\frac{1}{\gamma}=\frac{24-4K^2}{12+K^2} \tag{30}$$

and two parasites,

$$\gamma+\frac{1}{\gamma}=-4. \tag{31}$$

In the lossless case, the physical modes have $|\gamma|=1$ for all frequencies $W\leqslant\pi$. In Fig. 6 we plot $\hat{L}/L$ and δ for the physical modes. Comparison with Figs. 2 and 3 reveals enhanced accuracy, which we attribute to the smaller effective mesh spacing $a/\sqrt{2}$ and the quadratic local interpolation in this direction of the grid. The parasitic modes are independent of K and have the values $\gamma=-2\pm\sqrt{3}$. Their behavior is virtually the same as that of the triangular grid parasites. We conclude that the rules of thumb articulated above for the triangular grid are applicable in this idealized case as well: $W/\pi\leqslant 0.1$ and $WS\leqslant 0.02$.

Application of these guidelines to the properties listed in Table I yields maximum mesh spacings which appear in Table II. In every case except water, the constraint

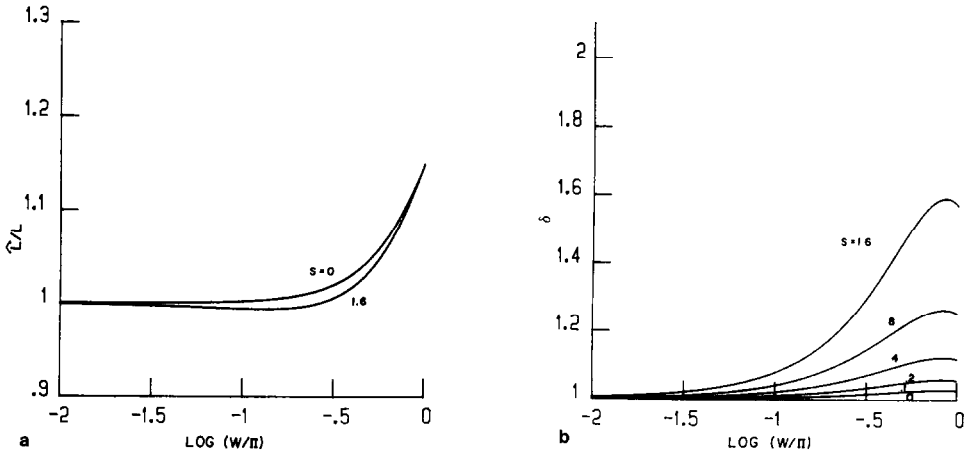

FIG. 6. Wavelength ratio (a) and damping ratio (b) for E_z wave in the 45° direction of the bilinear grid. $W = \omega a \sqrt{\mu\varepsilon}$; $S = \sigma a \sqrt{\mu/\varepsilon}$.

on WS dominates. A characteristic length for the torso is 30 cm, and resolution of internal tissue structure requires mesh spacings of roughly 1 cm or less. Thus as a first approximation we conclude that reasonable geometrical resolution will provide

TEST CASES

To test our method we have solved some simple 2-D cases where analytic solutions are available. The tests are motivated by two clinically available devices intended to produce noninvasive heating of deep-seated tumors, and the boundary conditions appropriate to each in the limiting planar case.

The first group of tests is inspired by the Annular Phased Array System (APAS) developed by the *BSD* Corporation (Salt Lake City, Utah). The physical charac-

TABLE II

Maximum Grid Spacing (m) for $WS \leqslant 0.02$, Based on the Tissue Properties of Table I

	13 MHz	40 MHz	70 MHz	100 MHz
Muscle	0.018	0.0096	0.0067	0.0053
Lung	0.167	0.021	0.01	0.0085
Fat	0.031	0.018	0.013	0.011
Bone	0.031	0.056	0.043	0.036
Heart	0.018	0.0091	0.0062	0.0052
Deionized water[a]	0.138	0.045	0.024	0.017

[a] For water the constraint is $W/\pi < 0.1$.

teristics and clinical experience with this device are summarized by Turner [36] and Gibbs *et al.* [6]. The patient torso, surrounded by a water bolus, is subjected to an incident electric field, polarized in the z direction (z being normal to the plane of analysis) by means of a series of apertures placed around the circumference. In this case, the simplified formulation (11) applies, and boundary conditions are by design of the Dirichlet type: E_z given at the device boundaries which enclose the patient. At internal boundaries where tissue properties change abruptly, E_z and ∇E_z are continuous, and thus (11) may be assembled without special care on simple C^0 elements. The matrix formulation of (11) is symmetric

$$[A]\{E_z\} = i\omega\mu\{F\} \tag{32}$$

with $A_{ij} = \langle \nabla\phi_i \cdot \nabla\phi_j - k^2\phi_i\phi_j \rangle$. We use a conventional banded solver with trivial modifications to handle complex numbers, which are represented as two floating-point 64-bit words each. Inner products are evaluated exactly on triangular elements, and by 2×2 Gauss quadrature on bilinear elements.

For an axisymmetric problem with uniform electric properties, the exact solution is

$$\frac{E_z(r)}{E_{z0}} = \frac{J_0(kr)}{J_0(kr_0)} \tag{33}$$

where r is the radial coordinate, E_{z0} is the imposed field at r_0, and J_0 is the Bessel function of the first kind. In Fig. 7 we compare this to our numerical solution obtained with the tissue properties of Table I at 70 MHz. The agreement is within 3.9% of E_{z0}. Improvements in either the radial resolution or the quadrature had

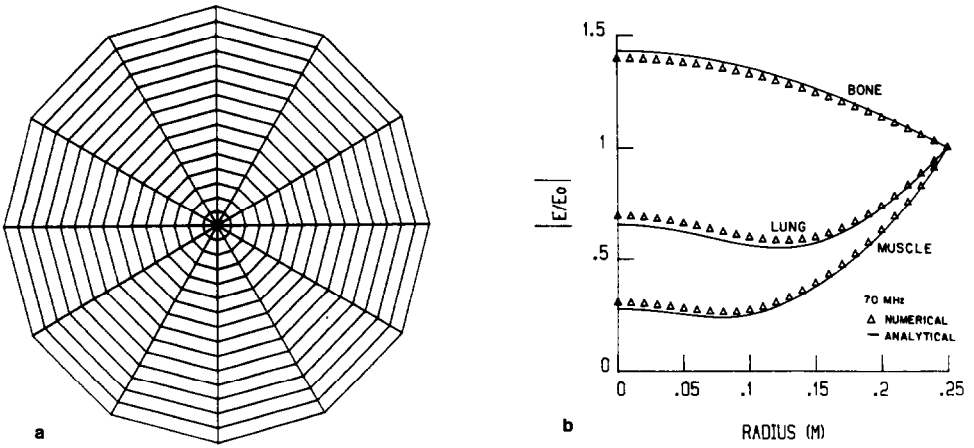

FIG. 7. (a) Finite element mesh for the cylinder test cases. $\Delta r = 1$ cm. (b) Electric field magnitude versus radius for uniform cylinder; Annular Phased Array System. Tissue properties are from Table I at 70 MHz.

minor impact on this error; doubling the circumferential resolution reduced the worst error to 1.1%. In all of these runs, circumferential variations were present in regular patterns, with negligible amplitude $\sim 10^{-5}$.

On the same mesh we have also solved the idealized case where distinct tissue types are arranged in concentric layers. The analytic solution in layer i is

$$E_z(r) = A_i J_0(kr) + B_i Y_0(kr) \tag{34}$$

where Y_0 is the Bessel function of the second kind. In addition to satisfying the usual boundary conditions, the A_i, B_i must also satisfy the continuity of E_z and $\partial E_z/\partial r$ at the interfaces. Results are shown in Fig. 8 at 70 MHz. The accuracy is comparable to that of Fig. 7.

The second device which we have studied is the Magnetrode, developed by Henry Medical Electronics Inc. (Los Angeles, Calif.). This is essentially a magnetic induction device in which the patient is surrounded by a current-carrying coil. Technical and clinical information is provided by Storm *et al.* [32] and Oleson [24].

For the limiting plane case we have $\mathbf{H} = H(x, y)\,\mathbf{z}$ and $\mathbf{E}$ confined to the (x, y) plane. At the device boundary, $H = J_s$, the amplitude of the current per unit length in the coil. We solve for $\mathbf{E}$ directly with the general formulation (6). The external boundary conditions are enforced via the surface integral:

$$\mathbf{F}_i = \oint \mathbf{H} \times \mathbf{n}\phi_i \, ds = J_s \oint \mathbf{z} \times \mathbf{n}\phi_i \, ds = J_s \oint \phi_i \, \mathbf{ds}. \tag{35}$$

Since we have two complex unknowns E_{xi} and E_{yi} at each node, this formulation requires more computational power than that tested above. An additional complication is the requirement that $\mathbf{E}$ be discontinuous along internal tissue boundaries.

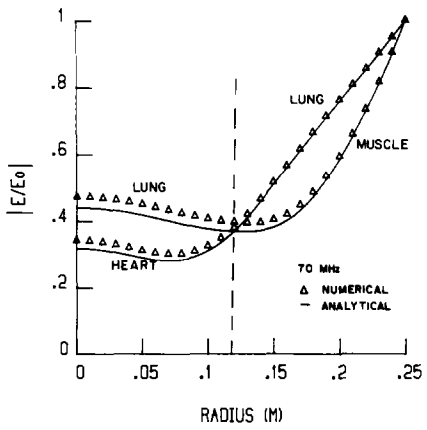

FIG. 8. Electric field magnitude for 2-material cylinder; Annular Phased Array System. The interface is at $r = 12$ cm.

We treat these internal boundaries by introducing a cut in the grid across which the interpolation of $\mathbf{E}$ is discontinuous, as in Fig. 9. Essentially we create separate grids for each tissue type, with coincident but distinct nodes along the interfaces. Denoting such a pair of nodes as 1 and 2, we assemble Galerkin equations 1 and 2 separately, in effect never carrying the inner products across an interface. Boundary conditions on nodes 1 and 2 are

$$\mathbf{n} \cdot (\varepsilon_{c1} \mathbf{E}_1 - \varepsilon_{c2} \mathbf{E}_2) = 0 \tag{36a}$$

$$\mathbf{n} \times (\mathbf{E}_1 - \mathbf{E}_2) = 0 \tag{36b}$$

$$\mathbf{n} \times (\mathbf{H}_1 - \mathbf{H}_2) = 0. \tag{36c}$$

$$\mathbf{n} \cdot (\mu_1 \mathbf{H}_1 - \mu_2 \mathbf{H}_2) = 0. \tag{36d}$$

In view of (36c), the internal boundary integrals $\mathbf{F}_1$ and $\mathbf{F}_2$ may be eliminated from the algebraic system by summing Galerkin equations 1 and 2. Equations (36a), (36b) then close the set, provided a suitable definition of $\mathbf{n}$ is available. In the tests reported here we adopt the "nodal normal," essentially a local average of the piecewise continuous $\mathbf{n}$

$$\mathbf{n}_i = \oint \mathbf{n} \phi_i \, ds \Big/ \oint \phi_i \, ds \tag{37}$$

which has been used successfully in other wave propagation studies [19, 20, 16] and also in parabolic problems [17]. Note, however, that this definition of $\mathbf{n}_i$ does not guarantee the vanishing of $\mathbf{E}_1^* \cdot \mathbf{F}_1 + \mathbf{E}_2^* \cdot \mathbf{F}_2$, and we anticipate some local numerical power loss or gain across tissue interfaces where the curvature is not well resolved by the grid.

The matrix formulation of (6) is

$$[A]\{E\} = i\omega\mu\{F\} \tag{38}$$

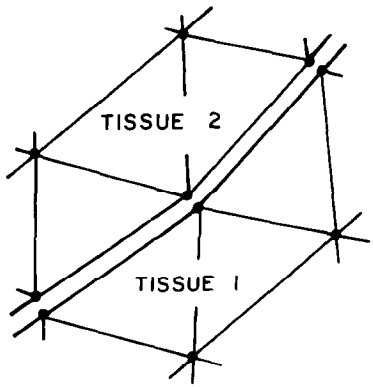

FIG. 9. Cut in element grid along a tissue interface.

where A, E, and F comprise the two-dimensional complex submatrices

$$A_{ij}=\begin{bmatrix} \left\langle \frac{\partial\phi_i}{\partial y}\frac{\partial\phi_j}{\partial y}\right\rangle - \langle k^2\phi_i\phi_j\rangle & \left\langle -\frac{\partial\phi_j}{\partial x}\frac{\partial\phi_i}{\partial y}\right\rangle \\ \left\langle -\frac{\partial\phi_j}{\partial y}\frac{\partial\phi_i}{\partial x}\right\rangle & \left\langle \frac{\partial\phi_i}{\partial x}\frac{\partial\phi_j}{\partial x}\right\rangle - \langle k^2\phi_i\phi_j\rangle \end{bmatrix},$$

$$E_j=\begin{Bmatrix} E_{xj} \\ E_{yj} \end{Bmatrix}, \tag{39}$$

$$F_i=J_s\begin{Bmatrix} \oint \phi_i\,dx \\ \oint \phi_i\,dy \end{Bmatrix}.$$

As in the simpler case above we use a complex banded matrix solver with the same level of precision and inner product quadrature.

For the axisymmetric test cases the exact solution for H_z is the same as for E_z in Eq. (34), with the requirement that H_z and $(1/\varepsilon_c)(\partial H_z/\partial r)$ be continuous at interfaces. The electric field is then given by

$$\mathbf{E}=\frac{1}{i\omega\varepsilon_c}\frac{\partial H_z}{\partial r}\boldsymbol{\phi} \tag{40}$$

where $\boldsymbol{\phi}$ is the circumferential unit vector. Solutions obtained on the grid of Fig. 7a, truncated at $r=15$ cm, are displayed in Figs. 10–12. In Fig. 10 we show $|\mathbf{E}|$ versus r for muscle at several frequencies. As expected, the accuracy degrades with increas-

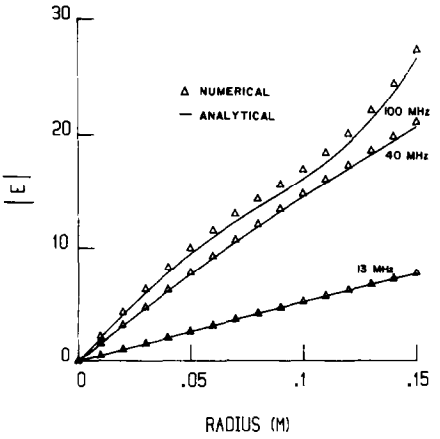

FIG. 10. Electric field magnitude for uniform cylinder of muscle tissue at various frequencies; Magnetrode.

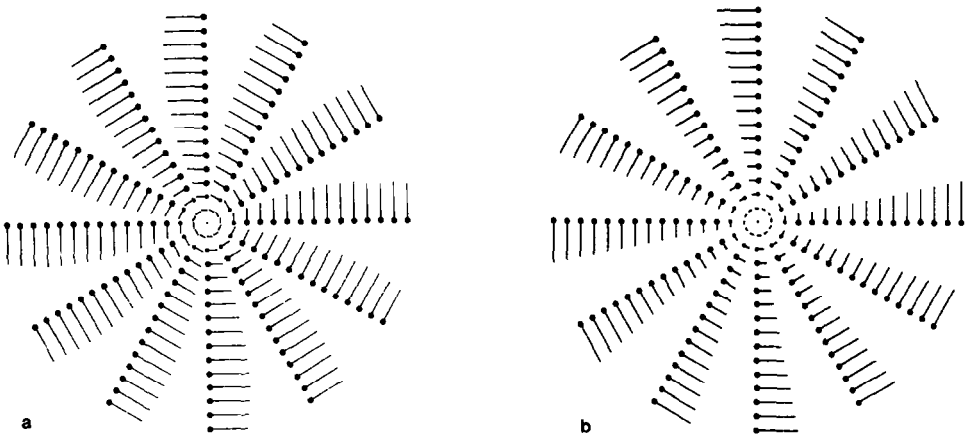

FIG. 11. Vector plots of **E** for muscle at 70 MHz; Magnetrode. (a) Re(**E**); (b) $-\text{Im}(\mathbf{E})$.

ing frequency, from 0.1% of $E_{\max}$ at 13 MHz to 3% at 70 (not shown) and 100 MHz. As in previous tests, $|E|$ is essentially uniform in the circumferential direction. Vector plots of Re(**E**) and Im(**E**) appear in Fig. 11 and display the proper circulation of **E** about the z axis. In Fig. 12 we show results for 3 different combinations of tissue. As expected from Table II, the case with the largest mass of muscle yields the largest error, 3.6%, while the other two cases are within 1% of the exact solution.

Since this formulation provides continuity of **E** and exact satisfaction of the interfacial jump conditions, we regard it as preferable for scientific work where precision is the only goal. In practice, however, we expect ultimately to implement these algorithms on small computers for routine treatment planning, and numerical com-

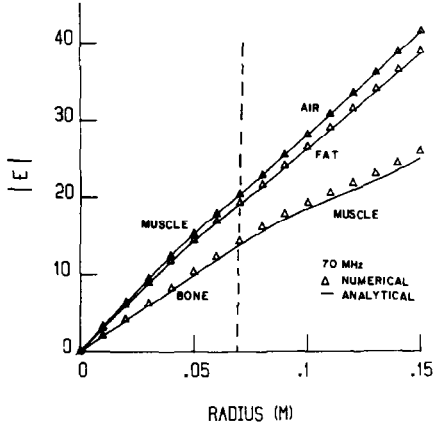

FIG. 12. Electric field magnitude for 2-material (muscle–air, muscle–fat, and bone–muscle) cylinders at 70 MHz; Magnetrode. The interface is at $r = 7$ cm.

plexity may become a limiting factor. We have therefore studied the numerically simpler but less elegant approach in which **H** is obtained on finite elements, and subsequently differentiated to obtain **E**. Since **H** in this problem is normal to the plane, its computation is essentially the same as in the simple formulation (11). We expect therefore to gain by a factor of 4 in matrix storage requirements, and by a factor of 8 in the operation count for direct solution. An additional factor of 2 [illegible] savings will only be marginally eroded by the additional operations required to differentiate **H**; the drawback is the resulting loss of accuracy in **E**, which will be discontinuous across all element boundaries.

The general formulation for **H** is readily obtained by retracing the steps from Eqs. (1) through (6). The result, analogous to (6), is

$$\left\langle \frac{1}{k^2}(\nabla \times \mathbf{H}) \times \nabla \phi_i \right\rangle - \langle \mathbf{H} \phi_i \rangle = \frac{1}{i\omega\mu} \oint \mathbf{E} \times \mathbf{n} \phi_i \, ds. \tag{41}$$

Note that $\mathbf{n} \times \mathbf{E}$ is continuous across tissue boundaries. When as in the induction heating case $\mathbf{H} = H_z(x, y)\,\mathbf{z}$, (41) simplifies to the analog of (11),

$$\left\langle \frac{1}{k^2} \nabla H_z \cdot \nabla \phi_i \right\rangle - \langle H_z \phi_i \rangle = \oint \frac{1}{k^2} \nabla H_z \cdot \mathbf{n} \phi_i \, ds. \tag{42}$$

With H_z given on the boundary in terms of the coil current, we solve (42) by minor modification of the algorithm tested above for the Annular Phased Array problems.

Results analogous to Fig. 12 appear in Fig. 13a, where we plot $|E|$ at element centers. In Fig. 13b we show the same calculations but with the circumferential

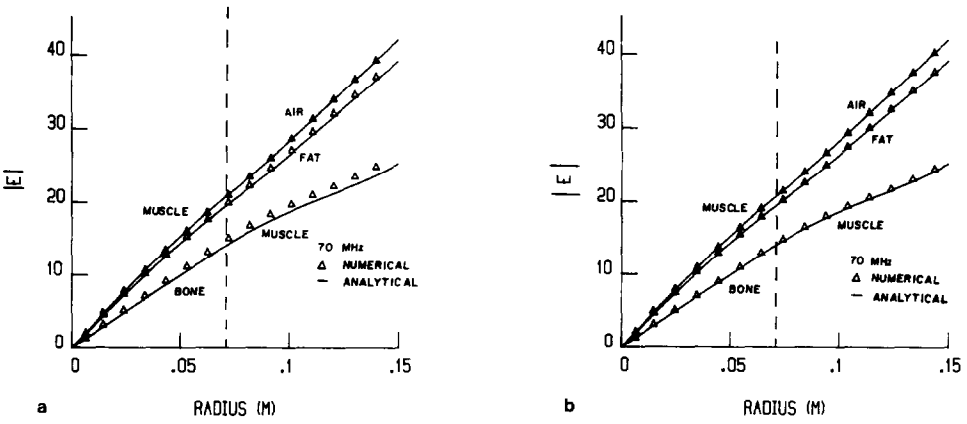

FIG. 13. Same as Fig. 12. Solution obtained from reduced formulation (42) and plotted at element centers.

resolution doubled. The accuracy at these points is quite satisfying in both cases: the worst error is roughly 4.6% in Fig. 13a, and 1.1% in Fig. 13b. Bear in mind, however, that this numerical solution is essentially piecewise constant in r. At present we are examining the impact of this on the thermal predictions, which are the ultimate goal of our project.

Example of Clinical Application

To illustrate the ultimate use of our algorithms, we present a realistic problem based on *CT* scans of typical cancer patients being treated at our institution. Figure 14a shows a thoracic cross section containing a tumor mass embedded deeply in the right lung. The finite element discretization appears in Fig. 14b for the thorax itself, and in Figs. 14c,d for the space between the APAS and solenoid devices and the patient. On these grids we calculated the appropriate field by

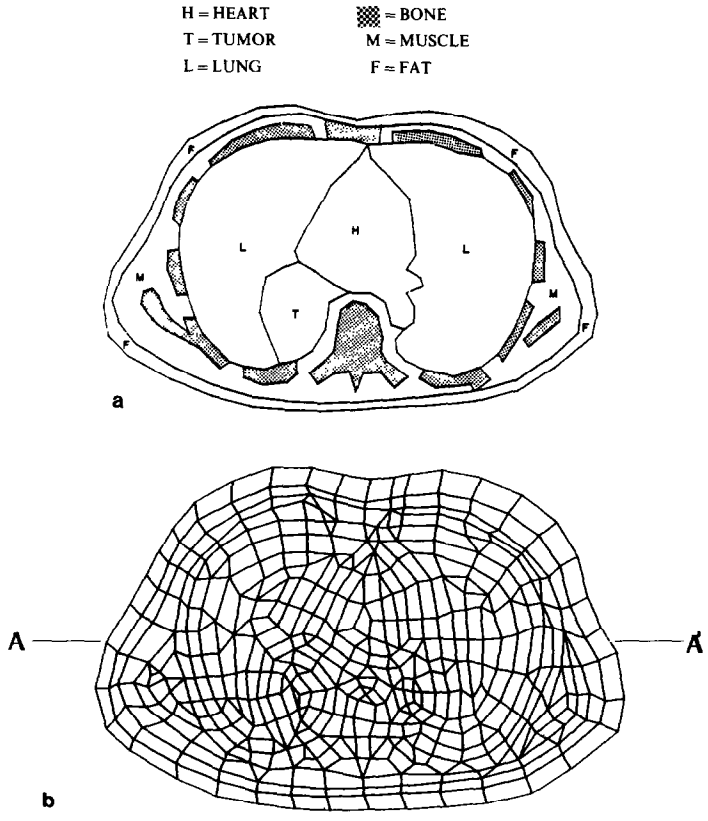

FIG. 14. (a) Representative thoracic cross section. (b) Finite element mesh for thorax.

Eq. (11) (APAS) or (42) (Magnetrode); $|\mathbf{E}|$ is reported in Figs. 15a,b along the line AA' of Fig. 14b. As expected, $|\mathbf{E}|$ generally decreases toward the patient center for the Magnetrode. The APAS results are relatively flat across the patient. Note that in the APAS case, since $\mathbf{E}$ is calculated at each node the plotted points were obtained via nodal interpolation. In the solenoid case $\mathbf{E}$ was only computed at the centroid of each element and the points plotted are the field value at the center of the element nearest the AA' axis.

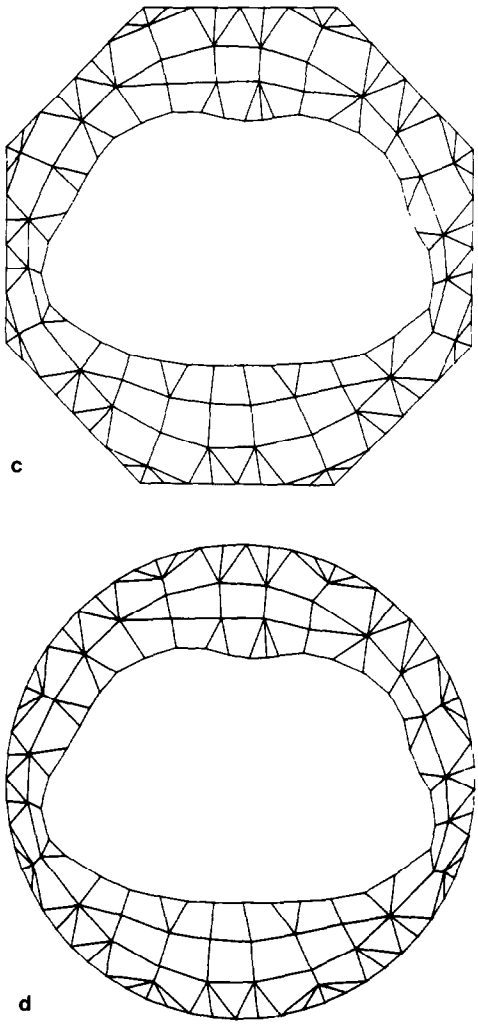

FIG. 14. (c) Finite element mesh for APAS simulation. (d) Finite element mesh for Magnetrode simulation.

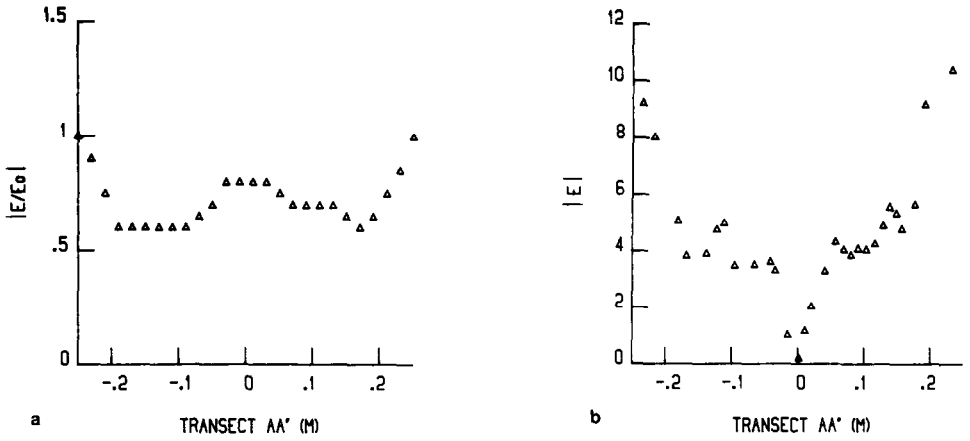

FIG. 15. $|\mathbf{E}|$ along the line AA' of Fig. 14b; (a) APAS, (b) Magnetrode.

CONCLUSION

Based on these tests, we are confident that our algorithms effectively solve Maxwell's equations under typical hyperthermia conditions. Presently we are using these algorithms to develop the distributed heat source for finite element thermal calculations [25]. Two issues remain open:

(a) *The propriety of* 2-D *calculations.* Obviously the general problem which we face is three-dimensional, and our formulations are posed in 3-D. We view the simpler plane calculation, as typified by the clinical example above, as a best case analysis—treatments which fail to produce satisfactory heating via this analysis are unlikely to perform better when analyzed in 3-D. At a minimum, then, the plane analysis may be used as a screening mechanism. The extent to which we can extrapolate good 3-D performance from good 2-D performance, and thus avoid computing the third dimension, remains an open question and one which we expect to report on in the future.

(b) *The level of spatial resolution required for practical purposes.* Since the ultimate thermal calculations involve significant diffusion, there is a level of resolution for $\mathbf{E}$ which need not be exceeded, and we hope to establish this in the future. For example, we expect but have not yet demonstrated that computed temperatures will be insensitive to the choice of formulation—Eq. (6) versus (42)—for solenoid-type devices.

Both of these issues are especially important as they determine ultimately the frequency of clinical use. The requirement of moderately large-scale, complex linear algebra on small machines is one potentially limiting factor; another is the level of sophistication required on input and output.

While we have assumed the magnetic permeability μ to be constant, the general Galerkin approach taken here is not limited to this case. With $\mu = \mu(\mathbf{x})$, the formulation (6) may be restated as

$$\left\langle \left(\frac{1}{i\omega\mu} \nabla \times \mathbf{E} \right) \times \nabla \phi_i \right\rangle + \langle i\omega\varepsilon_c \mathbf{E}\phi_i \rangle = \oint \mathbf{H} \times \mathbf{n}\phi_i \, ds \tag{43}$$

and its dual for the magnetic field is

$$\left\langle \left(\frac{1}{i\omega\varepsilon_c} \nabla \times \mathbf{H} \right) \times \nabla \phi_i \right\rangle + \langle i\omega\mu \mathbf{H}\phi_i \rangle = -\oint \mathbf{E} \times \mathbf{n}\phi_i \, ds. \tag{44}$$

Both have global conservation properties, and the dispersion analysis given herein for the homogeneous case applies. We are unaware of any precedent for this general formulation and look forward to applications in other areas.

ACKNOWLEDGMENTS

This work was supported in part by the National Science Foundation, Grant ECS-8307032, and by the National Cancer Institute, Grant CA 37245.

REFERENCES

1. H. F. BOWMAN, Thermodynamics of tissue heating: Modeling and measurements for temperature distributions, *in* "Physical Aspects of Hyperthermia" (G. H. Nussbaum, Ed.), pp. 511–548, Amer. Inst. Phys., New York, 1982.
2. E. C. BURDETTE, Electromagnetic and acoustic properties of tissues, *in* "Physical Aspects of Hyperthermia" (G. H. Nussbaum, Ed.), pp. 105–150, Amer. Inst. Phys., New York, 1982.
3. M. V. K. CHARI AND P. P. SILVESTER (Eds.), "Finite Elements in Electric and Magnetic Field Problems," Wiley, Chichester, 1980.
4. M. V. K. CHARI, Finite element solution of magnetic and electric field problems in electric machines and devices, *in* "Finite Elements in Electric and Magnetic Field Problems" (M. V. K. Chari and P. P. Silvester, Eds.), pp. 87–108, Wiley, Chichester, 1980.
5. L. A. DETHLESEN AND W. C. DEWEY (Eds.), "Third Int'l. Symp.: Cancer Therapy By Hyperthermia, Drugs, and Radiation," National Cancer Inst. Monograph 61, 1982.
6. F. A. GIBBS, JR., M. D. SAPOZINK, K. S. SETTLES, AND J. R. STEWART, *IEEE Trans. Biomed. Eng. BME* **31** (1984), 115.
7. W. G. GRAY AND D. R. LYNCH, *Adv. Water Resour.* **1** (2) (1977), 83.
8. A. W. GUY, J. F. LEHMANN, AND J. B. STONEBRIDGE, *Proc. IEEE* **62** (1974), 55.
9. G. M. HAHN, "Hyperthermia and Cancer," Plenum, New York, 1982.
10. G. M. HAHN, P. KERNAHAN, A. MARTINEZ, D. POUNDS, S. PRIONAS, T. ANDERSON, AND G. JUSTICE, *Ann. N.Y. Acad. Sci.* **335** (1980), 327.
11. S. C. HILL, D. A. CHRISTENSEN, AND C. H. DURNEY, *Int. J. Radiat. Oncol. Biol. Phys.* **9** (1983), 893.
12. M. F. ISKANDER, P. F. TURNER, J. B. DUBOW, AND J. KAO, *J. Microwave Power* **17** (1982), 175.
13. R. K. JAIN, Bioheat transfer: Mathematical models of thermal systems, *in* "Hyperthermia in Cancer Therapy" (F. K. Storm, Ed.), pp. 9–46, G. K. Hall Medical Publishers, Boston, 1983.
14. E. C. JORDAN AND K. G. BALMAIN, "Electromagnetic Waves and Radiating Systems," Prentice-Hall, Englewood Cliffs, N.J., 1968.

15. J. C. LIN, A. W. GUY, AND C. C. JOHNSON, *IEEE Trans.* **MTT-21** (1973), 791.
16. D. R. LYNCH, *in* "Proceedings, OCEANS '81," IEEE Pub. No. 81CH1685-7, pp. 810–814, 1981.
17. D. R. LYNCH, *J. Comput. Phys.* **47** (1982), 387.
18. D. R. LYNCH, Mass balance in shallow water simulations, *in* "Proceedings, Fifth International Symposium on Finite Element Methods in Flow Problems," Austin, Texas, January 1984, pp. 1–5.
19. D. R. LYNCH AND W. G. GRAY, *Comput. Fluids* **7** (1979), 207.
20. D. R. LYNCH AND W. G. GRAY, *J. Comput. Phys.* **36** (1980), 135.
21. J. A. MACBAIN, *Int. J. Numer. Methods Eng.* **19** (1983), 1033.
22. F. MELKES AND M. ZLAMAL, *Int. J. Numer. Methods Eng.* **19** (1983), 1053.
23. R. MULLEN AND T. BELYTSCHKO, *Int. J. Numer. Methods Eng.* **18** (1982), 11.
24. J. R. OLESON, *IEEE Trans. Biomed. Eng. BME* **31** (1984), 91.
25. K. D. PAULSEN, J. W. STROHBEHN, AND D. R. LYNCH, *Radiat. Res.* **100** (1984), 536.
26. G. W. PLATZMAN, *J. Comput. Phys.* **40** (1981), 36.
27. J. C. SABONNADIÈRE, Numerical analysis of eddy-current problems, *in* "Finite Elements in Electric and Magnetic Field Problems" (M. V. K. Chari and P. P. Silvester, Eds.), pp. 109–124, Wiley, Chichester, 1980.
28. H. P. SCHWAN AND K. R. FOSTER, *Proc. IEEE* **68** (1980), 104.
29. J. G. SHORT AND P. F. TURNER, *Proc. IEEE* **68** (1980), 133.
30. P. P. SILVESTER AND R. L. FERRARI, "Finite Elements for Electrical Engineers," Cambridge Univ. Press, London/New York, 1983.
31. F. K. STORM, (Ed.), "Hyperthermia in Cancer Therapy," G. K. Hall Medical Publishers, Boston, 1983.
32. F. K. STORM, W. H. HARRISON, R. S. ELLIOTT, AND D. L. MORTON, Physical aspects of localized heating by magnetic-loop induction, *in* "Hyperthermia in Cancer Therapy" (F. K. Storm, Ed.), Hall Med. Pub., Boston, 1983.
33. F. K. STORM, R. S. ELLIOTT, W. H. HARRISON, J. R. KAISER, AND D. L. MORTON, *J. Surg. Oncol.* **17**
34. C. STREFFER *et al.*, (Eds.), "Proc. 2nd Int'l Symp. on Cancer Therapy by Hyperthermia and Radiation," Essen, Federal Republic of Germany, June 2–4, 1977, Urban & Schwarzenberg, Baltimore, 1978.
35. J. W. STROHBEHN AND R. B. ROEMER, *IEEE Trans. Biomed. Eng. BME* **31** (1984), 136.
36. P. F. TURNER, *IEEE Trans. Biomed. Eng. BME* **31** (1984), 106.
37. J. H. YOUNG, M. T. WANG, AND I. A. BREZOVICH, *Electron. Lett.* **16** (1980), 358.